



Semnan University

Mechanics of Advanced Composite Structures

journal homepage: <http://MACS.journals.semnan.ac.ir>

Buckling Analysis of Sandwich Structures with Metamaterials Core Integrated by Graphene Nanoplatelets Reinforced Polymer Composite

Y. Shabani ^a, K. Khorshidi ^{b*} ^a Department of Mechanical Engineering, Faculty of Engineering, Arak University, Arak, 38156-88349, Iran^b Associate Professor of Mechanical Engineering, Faculty of Engineering, Arak University, Arak, 38156-88349, Iran

KEYWORDS

Sandwich structures;
Nanocomposites;
Graphene nanoplatelets;
Buckling analysis;
Metamaterials;

ABSTRACT

A study on buckling analysis of Marine sandwich panels for interior partition walls with multilayer graphene nanoplatelet (GPL)/polymer composite facesheets is presented in this paper. Three different shapes of square, honeycomb, and re-entrant cellular shape with negative poison ratio are considered for the core layer. It is assumed that facesheets be composed of a polymer matrix reinforced by graphene nanoplatelet (GPL). Halpin-Tsai's micromechanical approach is used to determine the effective Young's modulus of the top and bottom layers and the rule of mixture for effective Poisson's ratio and mass density. The wall sandwich plate is modeled based on a new fifth-order shear deformation theory. Hamilton principle is employed to obtain the governing differential equations of motions of plates. The accuracy of the proposed formula and results are verified and proven accurate by the high agreement with the available results in the literature. Based on our results, we indicated the effect of cell configurations of the cellular core on the critical buckling load of marine interior wall sandwich plates. Moreover, the effect of thickness, aspect ratios, graphene nanoplatelet weight fraction, and geometrical parameters on the critical buckling load by the use of Galerkin's method is illustrated. The findings of this research may be beneficial in creating more efficient engineering applications, especially in the marine and ship industries.

1. Introduction

There is a continuous demand in using sandwich structures due to the need for low-weight, high-performance structures in the industry[1, 2]. There has been a rapid increase in the use of sandwich structures in an array of applications, including ships, automobiles, aircraft, satellites, and wind energy systems[3-7]. The rising demand in the shipbuilding industry is because the use of sandwich structures may lead to substantially lower production costs, relatively shorter product delivery times, improved ship performance owing to a lower structural weight, and improved fatigue and corrosion characteristics [8]. In theory and experiment, it has been shown that adding even a very small amount of graphene to a pure polymer matrix improves its mechanical properties

dramatically[9-13]. Nanofillers, such as carbon nanotubes (CNTs)[14-16] and graphene platelets (GPLs)[17], have been introduced to reinforced structures for engineering purposes (i.e., keeping a relatively high stiffness while losing weight). in a new methodology for structure comparison and design, Palomba et al.[18] suggested the use of aluminum honeycomb sandwich structures (AHS) in place of common marine structures, owing to their lightweight and environmental friendliness. Honeycombs have been used successfully in sandwich construction since the middle of the 1940s[19]. A finite element method can be used for modeling and analyzing honeycomb sandwich panels, but the method requires many computations because it is difficult to mesh a whole structure[20]. In the present study, we used a method that simulates the sandwich cores with a solid orthogonal plate

* Corresponding author. Tel.: +98-86-32625720; Fax: +98-86-32625721
E-mail address: k-khorshidi@araku.ac.ir

to simplify the modeling of honeycomb, re-entrant, and rectangular core layers.

The buckling behavior of engineering structures made of the advanced materials mentioned above has been investigated by many researchers. The Chebyshev-Ritz method was used by Yang et al. [21] to determine the uniaxial, biaxial, and shear buckling loads of FG-GPLRC plates. Kiani [22] used the TSDT to study the thermal buckling and post-buckling behavior of FG-GPLRC plates. An isogeometric analysis was used to study the static buckling of porous plates FG-GPLRC by Li et al. [23]. Ji and Waas [24] introduced a finite element formulation for buckling analysis of thick sandwich panels. The study by Song et al. [25, 26] examines bending and buckling analyses for FG graphene-reinforced polymer plates by using the FSDT and Navier solutions. Modeling and analysis of the post-buckling behavior of graphene-reinforced composite (GRC) laminated plates are presented by Shen et al. [27]. Shahverdi et al.[28] investigated the post-buckling analysis of geometrically perfect/imperfect honeycomb core sandwich panels having graphene platelet (GPL) reinforced face sheets based on a general higher-order plate model. Thermal buckling analysis of annular/circular microplates, which are made from functionally graded Graphene nanoplatelets (GNPs) reinforced porous nanocomposite is presented by Arshid et al.[29].

In this study, the buckling analysis of sandwich walls in the interior portion of ships and switchboard rooms in marine applications with a three-shape Models core, including positive, zero, and negative Poisson's ratio, surrounded by reinforced composite faces are investigated. It is assumed that facesheets be composed of an epoxy matrix reinforced by GPLs. The effect of geometric parameters of the core layer, besides the aspect ratio, length-to-thickness ratio, and core-thickness-to-total-thickness ratio on critical buckling load for all models in research is conducted. In this regard, the Halpin-Tsai micromechanical approach and rule of a mixture are used to determine the effective mechanical properties of composite layers, and a new fifth-order shear deformation theory was employed to derive the governing equation of the marine sandwich walls. The Galerkin method is used to solve the equations and the accuracy of the formulation and introduced theory is assessed by comparing available results in the literature with the calculated critical buckling loads. The findings of this research may be beneficial in creating more efficient engineering applications, especially the wall structure of ship engine control rooms (ECR) and switchboard rooms (SBR).

2. Materials Properties Problem Formulation

The ship structures panel with length a , width b , and thickness h are considered. The core layer is covered by multilayer GPL/polymer nanocomposite facesheets in the paper. The composite material has uniform distribution (UD) pattern of graphene sheets through the thickness in the facesheets of the wall panels. The facesheets with the UD pattern consist of layers of the same GPL weight fraction, as shown in Figure 1. Considering the Halpin-Tsai model, the effective Young's moduli of the facesheets will be defined as follows[30]:

$$E^{t,b} = \left(\frac{3}{8} \frac{1+V_{GPL}\zeta_L\eta_L}{1-\zeta_L\eta_L} + \frac{5}{8} \frac{1+V_{GPL}\zeta_T\eta_T}{1-\zeta_T\eta_T} \right) E_m \quad (1)$$

$$\zeta_L = 2 \frac{l_{GPL}}{h_{GPL}} \quad (2)$$

$$\zeta_T = 2 \frac{w_{GPL}}{h_{GPL}} \quad (3)$$

$$\eta_L = \frac{E_{GPL}/E_m - 1}{E_{GPL}/E_m + \zeta_L} \quad (4)$$

$$\eta_T = \frac{E_{GPL}/E_m - 1}{E_{GPL}/E_m + \zeta_T} \quad (5)$$

where E_m , E_{GPL} , V_{GPL} , ζ_L and ζ_T are Young's modulus of the polymer matrix, Young's modulus of the GPLs, GPL volume fraction, and the parameters characterizing both the geometry and size of GPL nanofillers, respectively. Besides, w_{GPL} , h_{GPL} and l_{GPL} In ζ formulations are the average width, thickness, and length of the GPLs. The volume fraction of GPLs is defined as:

$$V_{GPL} = \frac{g_{GPL}}{g_{GPL} + \left(\frac{\rho_{GPL}}{\rho_m} \right) (1 - g_{GPL})} \quad (6)$$

where ρ_{GPL} and ρ_m are the mass densities of GPLs and polymer matrix, and g_{GPL} is GPL weight fraction in the nanocomposite facesheets. The effective Poisson's ratio (ν_c) and Mass density (ρ_c) of GPL/ polymer nanocomposite can be calculated by applying the rule of mixture:

$$\nu_c^{t,b} = V_{GPL}\nu_{GPL} + V_m\nu_m \quad (7)$$

$$\rho_c^{t,b} = V_{GPL}\rho_{GPL} + V_m\rho_m \quad (8)$$

where V and ν are the volume fraction and Poisson's ratio, respectively. The mass fraction of GNPs for UD pattern can be expressed as follows:

$$g_{GPL}(z) = g_{GPL}^* \quad (9)$$

Three different types of wall sandwich plates are considered: rectangular core cell plates (Type A), honeycomb core plates (Type B), and re-entrant core cell plates (Type C). The sandwich plate of Type A has an aluminum rectangular core cell, as shown in Figure 2. In all Types, h_c is the

thickness of the core, and h is the total thickness of the sandwich wall. In sandwich plate Type A, the Poisson's ratio of the core layer is equal to zero[31].

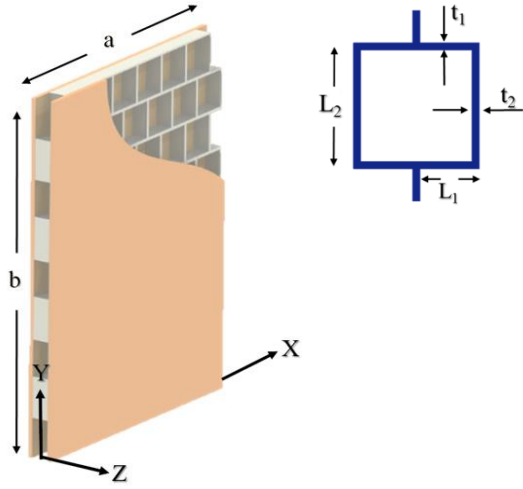


Fig. 1. Sandwich plate Type A with rectangular core cell

The Young's modulus (E), the shear elastic modulus (G), Poisson's ratios(ν), and density(ρ) of the rectangular core cell can be calculated from[31]:

$$E_{11}^c = E_s \frac{\gamma_3^3 \gamma_1}{1 + \gamma_3^2 \gamma_1} \quad (10)$$

$$E_{22}^c = E_s \frac{\gamma_3^3}{\gamma_1 + \gamma_3^2 \gamma_1} \quad (11)$$

$$G_{12}^c = E_s \frac{\gamma_3^3}{\gamma_1(1 + 2\gamma_1)} \quad (12)$$

$$G_{23}^c = G_s \frac{\gamma_3}{\gamma_1} \quad (13)$$

$$G_{31}^c = G_s \frac{\gamma_3}{2} \left[\frac{\gamma_1}{1 + 2\gamma_1} + \frac{1}{2} \right] \quad (14)$$

$$\nu_{12}^c = \nu_{21}^c = 0 \quad (15)$$

$$\rho^c = \rho_s \frac{\gamma_3(\gamma_1 + 2)}{2(\gamma_1)} \quad (16)$$

where $\gamma_1 = \frac{L_2}{L_1}$, $\gamma_2 = \frac{t_2}{t_1}$ and $\gamma_3 = \frac{t_1}{L_1}$ and superscript "c" represents core material. In the figures, L_1 is the length of the inclined cell rib, L_2 is the length of the vertical cell rib, and t is the rib thickness. Type B sandwich plates have an aluminum honeycomb core (Figure 2) that possesses a positive Poisson's ratio. The mechanical properties of the honeycomb core are defined in Eqs. 17-24.

$$E_{11}^c = E_s \frac{4\gamma_3^3(1 + 2\gamma_1)}{\sqrt{3}[3 + (1 + 4\gamma_1)\gamma_3^2]} \quad (17)$$

$$E_{22}^c = E_s \frac{4\sqrt{3}\gamma_3^3}{(2\gamma_1 + 1)(1 + 3\gamma_3^2)} \quad (18)$$

$$G_{12}^c = E_s \frac{2\gamma_3^3}{\gamma_1\sqrt{3}(1 + 2\gamma_1)} \quad (19)$$

$$G_{23}^c = G_s \frac{\gamma_3\sqrt{3}}{2\gamma_1 + 1} \quad (20)$$

$$G_{31}^c = G_s \frac{\gamma_3}{\sqrt{3}} \quad (21)$$

$$\nu_{12}^c = -\frac{(\gamma_3^2 - 1)(2\gamma_1 + 1)}{3 + (1 + 4\gamma_1)\gamma_3^2} \quad (22)$$

$$\nu_{21}^c = -\frac{3(\gamma_3^2 - 1)}{(1 + 3\gamma_3^2)(2\gamma_1 + 1)} \quad (23)$$

$$\rho^c = \rho_s \frac{\gamma_3(\gamma_1 + 2)}{\sqrt{3}(\gamma_1 + 0.5)} \quad (24)$$

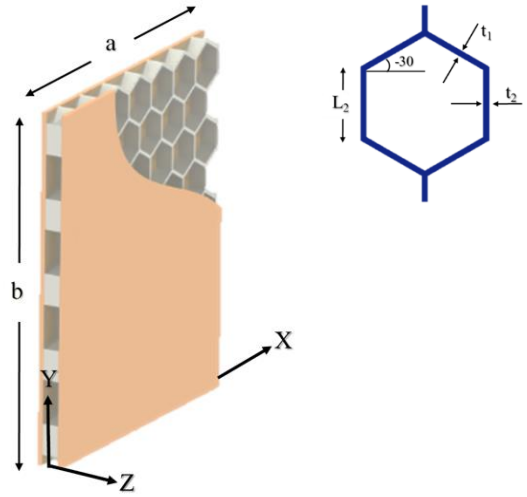


Fig. 2. Sandwich plate Type B with honeycomb core cell

Figure 3 indicates wall sandwich plate Type C, where the middle layer of this type is made of metamaterial re-entrant cells with negative Poisson's ratio. The mechanical properties of the core of Type C are described in Eqs. (25-32):

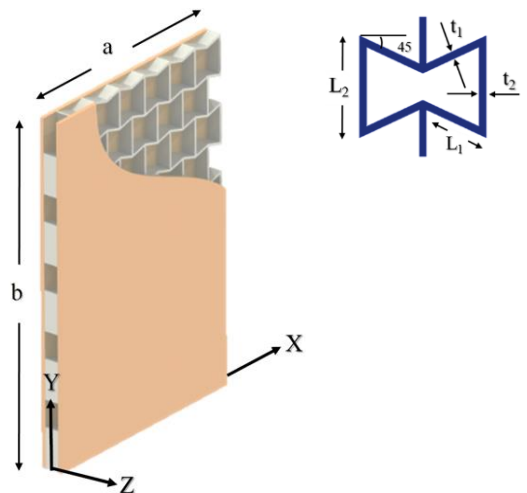


Fig. 3. Sandwich plate Type C with re-entrant core cell

$$E_{11}^c = E_s \frac{2\gamma_3^3(-1 + \sqrt{2}\gamma_1)}{1 + (1 + 2\gamma_1)\gamma_3^2} \quad (25)$$

$$E_{22}^c = E_s \frac{\sqrt{2}\gamma_3^3}{\left(\gamma_1 - \frac{\sqrt{2}}{2}\right)(1 + \gamma_3^2)} \quad (26)$$

$$G_{12}^c = E_s \frac{\sqrt{2}\gamma_3^3}{\gamma_1(1 + 2\gamma_1)} \quad (27)$$

$$G_{23}^c = G_s \frac{\sqrt{2}\gamma_3}{\sqrt{2} - 2\gamma_1} \quad (28)$$

$$G_{31}^c = G_s \frac{\gamma_3(-2 + (-3 + 2\sqrt{2})\gamma_1 - 4\gamma_1^2)}{\sqrt{2}(\sqrt{2} - 2\gamma_1)(1 + 2\gamma_1)} \quad (29)$$

$$v_{12}^c = -\frac{(\sqrt{2} - 2\gamma_1)(\gamma_3^2 - 1)}{\sqrt{2}(1 + (1 + 2\gamma_1)\gamma_3^2)} \quad (30)$$

$$v_{21}^c = -\frac{\sqrt{2}(\gamma_3^2 - 1)}{(1 + \gamma_3^2)(\sqrt{2} - 2\gamma_1)} \quad (31)$$

$$\rho^c = \rho_s \frac{\sqrt{2}\gamma_3(\gamma_1 + 2)}{\sqrt{2} - 2\gamma_1} \quad (32)$$

In all types, the Cartesian coordinate system (x,y,z) is assumed at the corner of the mid-plane of the panel.

3. Governing Equation

The constitutive equations of the marine sandwich panels can be written based on Hook's law as [32]:

$$\begin{bmatrix} \sigma_x \\ \sigma_y \\ \sigma_{xy} \end{bmatrix} = \begin{bmatrix} Q_{11}^{(k)} & Q_{12}^{(k)} & 0 \\ Q_{21}^{(k)} & Q_{22}^{(k)} & 0 \\ 0 & 0 & Q_{66}^{(k)} \end{bmatrix} \begin{bmatrix} \varepsilon_{xx} \\ \varepsilon_{yy} \\ \gamma_{xy} \end{bmatrix}, \quad (33)$$

$$\begin{bmatrix} \sigma_{yz} \\ \sigma_{xz} \end{bmatrix} = \begin{bmatrix} Q_{44}^{(k)} & 0 \\ 0 & Q_{55}^{(k)} \end{bmatrix} \begin{bmatrix} \gamma_{yz} \\ \gamma_{xz} \end{bmatrix}$$

$$\begin{aligned} Q_{11}^{(k)} &= \frac{E_{11}^{(k)}}{1 - \nu_{12}^{(k)}\nu_{21}^{(k)}} & Q_{12}^{(k)} &= \frac{\nu_{12}E_{11}^{(k)}}{1 - \nu_{12}^{(k)}\nu_{21}^{(k)}} \\ Q_{22}^{(k)} &= \frac{E_{22}^{(k)}}{1 - \nu_{12}^{(k)}\nu_{21}^{(k)}} & Q_{66}^{(k)} &= G_{12}^{(k)} \\ Q_{55}^{(k)} &= G_{13}^{(k)} & Q_{44}^{(k)} &= G_{23}^{(k)} \end{aligned} \quad (34)$$

In equations 33 and 34, stress(σ) is related to the strain(ε, γ) with stiffness coefficients(Q). Superscript (k) refers to the layer of the sandwich plate. k=t,c, and b denote the top layer, core layer, and bottom layer, respectively. The displacement field of wall sandwich plates based on a new fifth-order shear deformation theory is represented as:

$$U(x,y,z,t) = u(x,y,t) + G(z) \frac{\partial w(x,y,t)}{\partial x} + F(z)\xi(x,y,t) \quad (35)$$

$$V(x,y,z,t) = v(x,y,t) + G(z) \frac{\partial w(x,y,t)}{\partial x} + F(z)\psi(x,y,t) \quad (36)$$

$$W(x,y,z,t) = w(x,y,t) \quad (37)$$

where u(x,y,t), v(x,y,t) and w(x,y,t) are mid-plane displacement in the x, y, and z directions, ξ(x,y,t) and ψ(x,y,t) are denoted for rotation of the mid-surface around the x and y axes, respectively[33]. In addition, G(z) and F(z) are $G(z) = -z$, $F(z) = \left(\frac{19z}{22} - \frac{9z^3}{4h^2} + \frac{29z^5}{11h^4}\right)$. Linear strain-displacement relations are given by:

$$\varepsilon_x = \frac{\partial u}{\partial x} + G(z) \frac{\partial^2 w}{\partial x^2} + F(z) \frac{\partial \xi}{\partial x} \quad (38)$$

$$\varepsilon_y = \frac{\partial v}{\partial y} + G(z) \frac{\partial^2 w}{\partial y^2} + F(z) \frac{\partial \psi}{\partial y} \quad (39)$$

$$\gamma_{xy} = \left(\frac{\partial u}{\partial y} + \frac{\partial v}{\partial x}\right) + 2G(z) \frac{\partial^2 w}{\partial x \partial y} + F(z) \left(\frac{\partial \xi}{\partial y} + \frac{\partial \psi}{\partial x}\right) \quad (40)$$

$$\gamma_{xz} = \frac{\partial G(z)}{\partial z} \frac{\partial w}{\partial x} + \xi \frac{\partial F(z)}{\partial z} + \frac{\partial w}{\partial x} \quad (41)$$

$$\gamma_{yz} = \frac{\partial G(z)}{\partial z} \frac{\partial w}{\partial y} + \psi \frac{\partial F(z)}{\partial z} + \frac{\partial w}{\partial y} \quad (42)$$

The distribution of transverse shear stress along the thickness of the structure for Trigonometric theory(TSDPT)[34], Hyperbolic theory(HSDPT)[35, 36], Parabolic theory(PSDPT)[37], and the present introduced theory is illustrated in Fig 4. The modified shear deformation theory satisfies free stress conditions at z = -h/2 and the z = h/2 surfaces of the plate. The governing equations are extracted based on Hamilton's principle [38, 39]:

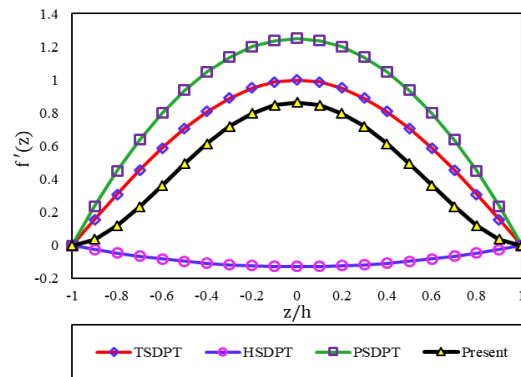


Fig. 4. A comparison of transverse shear stress distributions of the plate based on various theories

$$\int_0^t (\delta T - \delta U_s + \delta W) dt = 0 \quad (43)$$

where Us, T, and W refer to strain, kinetic, and work done by external non-conservative forces. Also, δ and t are the variation operator and time. The variation of strain energy of the wall sandwich plates with GPL-RC facesheets is calculated as follows[40]:

$$Us = \frac{1}{2} \int_V \sigma_{ij} \varepsilon_{ij} dV = \frac{1}{2} \int_V (\sigma_x \varepsilon_x + \sigma_y \varepsilon_y + \sigma_{xy} \gamma_{xy} + \sigma_{xz} \gamma_{xz} + \sigma_{yz} \gamma_{yz}) dV \quad (44)$$

$$\delta Us = \frac{1}{2} \int_S \left[(-\delta u \left(\frac{\partial N_{xx}}{\partial x} + \frac{\partial N_{xy}}{\partial y} \right) - \delta v \left(\frac{\partial N_{yy}}{\partial y} + \frac{\partial N_{xy}}{\partial x} \right) - \delta \xi \left(\frac{\partial P_{xx}}{\partial x} + \frac{\partial P_{xy}}{\partial y} - Q_{xz} \right) + \delta w \left(\frac{\partial^2 M_{xx}}{\partial x^2} + 2 \frac{\partial^2 M_{xy}}{\partial x \partial y} + \frac{\partial^2 M_{yy}}{\partial y^2} - \frac{\partial T_{yz}}{\partial y} - \frac{\partial T_{xz}}{\partial x} \right) - \delta \psi \left(\frac{\partial P_{xy}}{\partial x} + \frac{\partial P_{yy}}{\partial y} - Q_{yz} \right) \right] ds \quad (45)$$

where

$$(N_{xx}, N_{yy}, N_{xy}) = \int_{-\frac{h_c}{2} - (h_b + \frac{h_c}{2})}^{-\frac{h_c}{2}} (\sigma_x^b, \sigma_y^b, \sigma_{xy}^b) dz + \int_{-\frac{h_c}{2}}^{\frac{h_c}{2}} (\sigma_x^c, \sigma_y^c, \sigma_{xy}^c) dz + \int_{\frac{h_c}{2} + h_t}^{h_t} (\sigma_x^t, \sigma_y^t, \sigma_{xy}^t) dz \quad (46)$$

$$(M_{xx}, M_{yy}, M_{xy}) = \int_{-\frac{h_c}{2} - (h_b + \frac{h_c}{2})}^{-\frac{h_c}{2}} (\sigma_x^b, \sigma_y^b, \sigma_{xy}^b) G(z) dz + \int_{-\frac{h_c}{2}}^{\frac{h_c}{2}} (\sigma_x^c, \sigma_y^c, \sigma_{xy}^c) G(z) dz + \int_{\frac{h_c}{2} + h_t}^{h_t} (\sigma_x^t, \sigma_y^t, \sigma_{xy}^t) G(z) dz \quad (47)$$

$$(P_{xx}, P_{yy}, P_{xy}) = \int_{-\frac{h_c}{2} - (h_b + \frac{h_c}{2})}^{-\frac{h_c}{2}} (\sigma_x^b, \sigma_y^b, \sigma_{xy}^b) F(z) dz + \int_{-\frac{h_c}{2}}^{\frac{h_c}{2}} (\sigma_x^c, \sigma_y^c, \sigma_{xy}^c) F(z) dz + \int_{\frac{h_c}{2} + h_t}^{h_t} (\sigma_x^t, \sigma_y^t, \sigma_{xy}^t) F(z) dz \quad (48)$$

$$(Q_{xz}, Q_{yz}) = \int_{-\frac{h_c}{2} - (h_b + \frac{h_c}{2})}^{-\frac{h_c}{2}} (\sigma_{xz}^b, \sigma_{yz}^b) \frac{\partial F(z)}{\partial z} dz + \int_{-\frac{h_c}{2}}^{\frac{h_c}{2}} (\sigma_{xz}^c, \sigma_{yz}^c) \frac{\partial F(z)}{\partial z} dz + \int_{\frac{h_c}{2} + h_t}^{h_t} (\sigma_{xz}^t, \sigma_{yz}^t) \frac{\partial F(z)}{\partial z} dz \quad (49)$$

$$(T_{xz}, T_{yz}) = \int_{-\frac{h_c}{2} - (h_b + \frac{h_c}{2})}^{-\frac{h_c}{2}} (\sigma_{xz}^b, \sigma_{yz}^b) \left(\frac{\partial G(z)}{\partial z} + 1 \right) dz + \int_{-\frac{h_c}{2}}^{\frac{h_c}{2}} (\sigma_{xz}^c, \sigma_{yz}^c) \left(\frac{\partial G(z)}{\partial z} + 1 \right) dz + \int_{\frac{h_c}{2} + h_t}^{h_t} (\sigma_{xz}^t, \sigma_{yz}^t) \left(\frac{\partial G(z)}{\partial z} + 1 \right) dz \quad (50)$$

the total variation in kinetic energy is calculated as follows [41, 42]:

$$T = \frac{1}{2} \int_V [\dot{U}^2 + \dot{V}^2 + \dot{W}^2] \rho dV \quad (51)$$

$$\delta T = \frac{1}{2} \int_S \left[-\delta u \left(\ddot{u} I_1 + I_5 \ddot{\xi} + I_4 \frac{\partial \dot{w}}{\partial x} \right) - \delta v \left(I_1 \ddot{v} + I_5 \ddot{\psi} + I_4 \frac{\partial \dot{w}}{\partial y} \right) + \delta w \left(-I_1 \ddot{w} + I_2 \frac{\partial^2 \dot{w}}{\partial y^2} + I_2 \frac{\partial^2 \dot{w}}{\partial x^2} + I_4 \frac{\partial \dot{u}}{\partial x} + I_4 \frac{\partial \dot{v}}{\partial y} + I_6 \frac{\partial \dot{\psi}}{\partial y} + I_6 \frac{\partial \dot{\xi}}{\partial x} \right) - \delta \xi \left(I_3 \ddot{\xi} + I_5 \ddot{u} + I_6 \frac{\partial \dot{w}}{\partial x} \right) - \delta \psi \left(I_3 \ddot{\psi} + I_5 \ddot{v} + I_6 \frac{\partial \dot{w}}{\partial y} \right) \right] ds \quad (52)$$

where $I_1, I_2, I_3, I_4, I_5,$ and I_6 are the inertia coefficients calculated from:

$$I_j = \int_{-\frac{h_c}{2} - (h_b + \frac{h_c}{2})}^{-\frac{h_c}{2}} \rho^b J_j dz + \int_{-\frac{h_c}{2}}^{\frac{h_c}{2}} \rho^c J_j dz + \int_{\frac{h_c}{2} + h_t}^{h_t} \rho^t J_j dz \quad (53)$$

$$J_j = \left(1, (G(z))^2, (F(z))^2, G(z), F(z), F(z) \cdot G(z) \right) \quad (54)$$

where ρ is the mass density of each layer. Employing Hamilton's principle, the equations of motion for the three-layer wall sandwich plate can be written as:

$$\delta u: \frac{\partial N_{xx}}{\partial x} + \frac{\partial N_{xy}}{\partial y} = \ddot{u} I_1 + I_5 \ddot{\xi} + I_4 \frac{\partial \dot{w}}{\partial x} \quad (55)$$

$$\delta v: \frac{\partial N_{yy}}{\partial y} + \frac{\partial N_{xy}}{\partial x} = I_1 \ddot{v} + I_5 \ddot{\psi} + I_4 \frac{\partial \dot{w}}{\partial y} \quad (56)$$

$$\delta w: \frac{\partial T_{yz}}{\partial y} + \frac{\partial T_{xz}}{\partial x} - \frac{\partial^2 S_{xx}}{\partial x^2} - 2 \frac{\partial^2 S_{xy}}{\partial x \partial y} - \frac{\partial^2 S_{yy}}{\partial y^2} = I_1 \ddot{w} - I_2 \left(\frac{\partial^2 \dot{w}}{\partial y^2} + \frac{\partial^2 \dot{w}}{\partial x^2} \right) - I_4 \left(\frac{\partial \dot{u}}{\partial x} + \frac{\partial \dot{v}}{\partial y} \right) - I_6 \left(\frac{\partial \dot{\psi}}{\partial y} + \frac{\partial \dot{\xi}}{\partial x} \right) \quad (57)$$

$$\delta \xi: \frac{\partial P_{xx}}{\partial x} + \frac{\partial P_{xy}}{\partial y} - Q_{xz} = I_3 \ddot{\xi} + I_5 \ddot{u} + I_6 \frac{\partial \dot{w}}{\partial x} \quad (58)$$

$$\delta \psi: \frac{\partial P_{xy}}{\partial x} + \frac{\partial P_{yy}}{\partial y} - Q_{yz} = I_3 \ddot{\psi} + I_5 \ddot{v} + I_6 \frac{\partial \dot{w}}{\partial y} \quad (59)$$

3.1. Analytical Solution

In this section for achieving the critical buckling load of Sandwich plates used on marine interior walls, the Galerkin method is implemented. The following admissible functions which satisfy the simply supported boundary conditions are used to approximate the displacement field [43].

$$u = \sum_{m=1}^M \sum_{n=1}^N u_{m,n} \cos\left(\frac{n\pi x}{a}\right) \sin\left(\frac{m\pi y}{b}\right) e^{i\omega t} \quad (60)$$

$$v = \sum_{m=1}^M \sum_{n=1}^N v_{m,n} \sin\left(\frac{n\pi x}{a}\right) \cos\left(\frac{m\pi y}{b}\right) e^{i\omega t} \quad (61)$$

$$w = \sum_{m=1}^M \sum_{n=1}^N w_{m,n} \sin\left(\frac{n\pi x}{a}\right) \sin\left(\frac{m\pi y}{b}\right) e^{i\omega t} \quad (62)$$

$$\xi = \sum_{m=1}^M \sum_{n=1}^N \xi_{m,n} \cos\left(\frac{n\pi x}{a}\right) \sin\left(\frac{m\pi y}{b}\right) e^{i\omega t} \quad (63)$$

$$\psi = \sum_{m=1}^M \sum_{n=1}^N \psi_{m,n} \sin\left(\frac{n\pi x}{a}\right) \cos\left(\frac{m\pi y}{b}\right) e^{i\omega t} \quad (64)$$

In Eqs.(60-64) , $u_{m,n}$, $v_{m,n}$, $w_{m,n}$, $\xi_{m,n}$, and $\psi_{m,n}$ are unknown coefficients, m and n are the numbers of half-waves of mode shapes in the x and y directions. By multiplying governing equations by trial functions and integrating over the domains and using equation 65, the critical buckling load can be reached.

$$([K] - N_{cr}[M])\{\Gamma\} = 0 \quad (65)$$

where $[K]$ and $[M]$ refer to the stiffness and buckling matrix, respectively, $\{\Gamma\}$ is the vector of unknown coefficients and N_{cr} is the buckling parameter for the sandwich plate in the marine structure.

4. Results and Discussion

In this section, numerical results are presented to examine the effect of various parameters on the critical buckling load of the GPLRC. Material properties of facesheets are considered as $E_M = 3.0$ (GPa), $\nu_m = 0.34$, and $\rho_m = 1.2$ (g/cm³) for epoxy and $E_{GPL} = 3.0$ (GPa), $\nu_{GPL} = 0.34$, and $\rho_{GPL} = 1.2$ (g/cm³) for GPLs. To verify the accuracy of the presented solution consider a simply supported GPLRC plate of $b=0.4$ (m), $h/b=0.1$, and $a/b=1$ reinforced with GPLs of $w_{GPL} = 1.5$ (μm), $l_{GPL} = 2.5$ (μm), and $h_{GPL} = 1.5$ (μm). For different GPL weight fraction g_{GPL}^* dimensionless critical buckling (N_{cr}) load plates under uniaxial ($\beta_1 = -1$, $\beta_2 = 0$) and equal biaxial ($\beta_1 = -1$, $\beta_2 = -1$) compressions is presented in Table 1.

The dimensionless definition is considered as $\bar{N}_{cr} = \frac{N_{cr} a^2}{E_m H^3}$ in table 1 and the percentage below each value represents the difference with the critical buckling load of pure epoxy. As you can see in Table 1, a good agreement for different g_{GPL}^* is observed between the present work and the obtained results by Song et al [26].

Parametric studies have been conducted on the effects of the wall sandwich plate aspect ratio (a/b), plate thickness-to-width ratio (H/b), and GPL weight fraction (g_{GPL}^*) on the dimensionless

critical buckling load. The effects of these parameters were investigated for three Types of ship partition wall sandwich plates: rectangular core cell plates (Type A), Honeycomb core plates (Type B), and re-entrant core cell plates (Type C). The geometric parameters are chosen as follows, the lengths $a=b$, $t_1=t_2$, $t_1=0.001$ m, $h=0.02$ m. The core of the sandwich plate is made of aluminum, and its modulus is $E_s = 69$ GPa, the shear modulus is $G_s = 26$ GPa, Poisson's ratio is $\nu_s=0.33$, and density $\rho_s = 2700$ kg/m³ and dimensionless definition of critical buckling load is assumed as $\bar{N}_{cr} = \frac{N_{cr} a^2}{E_m H^3}$. Figure 5. shows the effect of cellular parameters on dimensionless critical buckling load of wall sandwich plates with $h_c/H=0.6$ in three cases: rectangular core cell plates (Type A), honeycomb core plates (Type B), and re-entrant core cell plates (Type C).

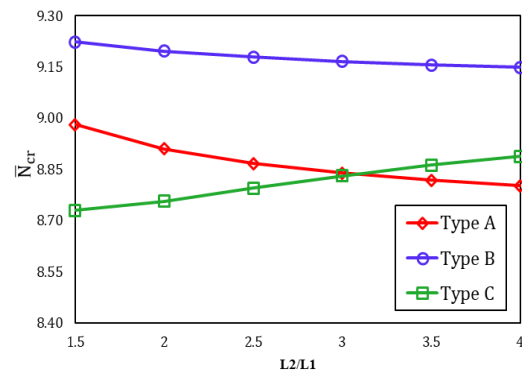


Fig. 5. The effect of vertical to inclined cell rib length on the dimensionless critical buckling load of sandwich ship partition

The results show that the lower ratio of L_2/L_1 decreases the dimensionless critical buckling load of the plates with honeycomb (Type B) and Auxetic (Type C) cores. On the contrary, in Type A with a rectangular core by changing the length of the vertical to inclined cell rib ratio (L_2/L_1) dimensionless critical buckling load increases. As shown in Figure 5, the dimensionless critical buckling load of plates Types A and C around $L_2/L_1=3$ are the same. It means it is possible to reach a similar critical buckling load by changing the core cellular shape.

In Figure 6, the effects of the aspect ratio (a/b) on the dimensionless critical buckling load of all three types are shown ($\gamma_1=2$, $h_c/H=0.6$). It is shown that with an increase in the aspect ratio (a/b), the dimensionless critical buckling load decreases. It is illustrated that in general, there aren't many differences between them but in low aspect ratios the dimensionless critical buckling load of plates with re-entrant cell shape core is higher than those of the other two types, and in low ratios, it is the opposite.

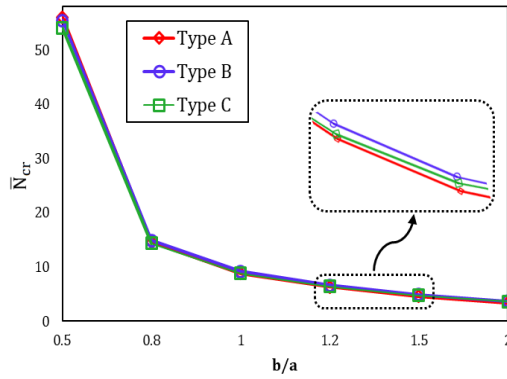


Fig. 6. The effects of the aspect ratio(a/b) on the dimensionless critical buckling load of sandwich ship walls

Figure 7 compares the dimensionless critical buckling load, \bar{N}_{cr} , versus length-to-thickness ratio, a/H ; which shows that with an increase in the length-to-thickness ratio (constant length and thickness decrease), the dimensionless critical buckling load increases. Figure 7 also shows that at a low length-to-thickness ratio (a/H), the critical buckling load of Type C is greater than that of Type A. As the length-to-thickness ratio (a/H) increases, the critical buckling load of plates types B and C rises more than for plates types A.

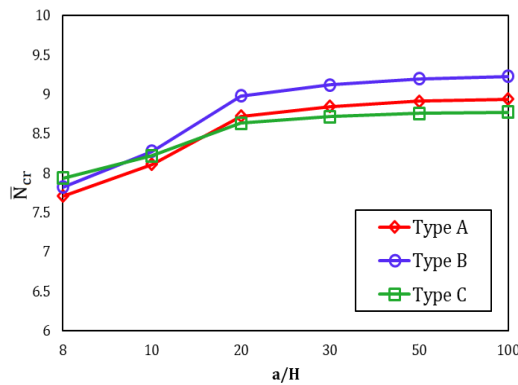


Fig. 7. The effects of the length-to-thickness ratios(a/H) on the dimensionless critical buckling load of sandwich ship walls

In Figure 8, the length-to-thickness ratio is assumed as $h/b=0.02$, $g_{GPL}^* = 0.6\%$, $\frac{h_{GPL}}{l_{GPL}} = \frac{w_{GPL}}{l_{GPL}} = 6 \times 10^{-4}$, $\gamma_1 = 2$ and hc indicates the thickness of the core layer. The dimensionless critical buckling loads of all Types at the beginning of the graph are close to each other because the facesheets are more effective than the core at low hc/h ratios. In both Figures 8 and 9 according to the assumption, the dimensionless critical buckling load of panel type C is less than

type A, and Type A less than Type B. the dimensionless critical buckling load of panel type B is higher than others due to the effect of the honeycomb core. It can also be seen in Figure 8 that values of the critical buckling load in uniaxial loading are higher than corresponding ones of biaxial loading which is an evident conclusion. The effect of the width and thickness of the GNPs on the critical buckling load of sandwich ship walls is illustrated in Figure 9. In figure 9, similar to figure 8, panel type B has a higher dimensionless critical buckling load than the two other types due to its core properties. The average length of GPL nanofillers IGPL is kept constant and other assumptions for the plates are similar to figure 8. Figure 9 displays that an increase in the width of GNPs leads to a rise in the values of the critical buckling load. Furthermore, the figure demonstrates that increasing the thickness of GNPs lowers the values of critical buckling load. Therefore, in order to have better reinforcing effects, it will be necessary to use graphene nanoparticles with a higher surface area and fewer monolayer graphene sheets.

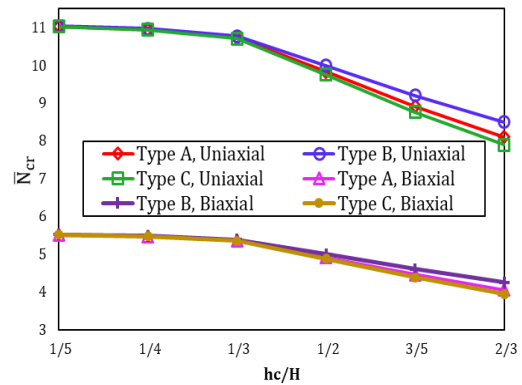


Fig. 8. The effects of the core thickness to total thickness ratios(hc/H) on the dimensionless critical biaxial and uniaxial buckling load of sandwich ship walls

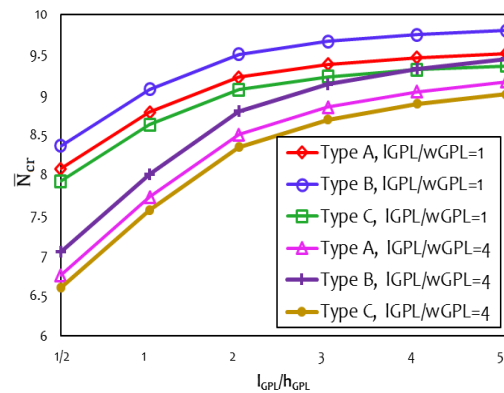


Fig. 9. The effects of GPL length-to-thickness and length-to-width ratios on the dimensionless critical buckling load of sandwich ship walls

Table 1. Comparisons of dimensionless critical buckling loads of GPL/epoxy plates under uniaxial and equal biaxial compressions

		Pure Epoxy	$g_{GPL}^* = 0.2\%$	$g_{GPL}^* = 0.4\%$	$g_{GPL}^* = 0.6\%$	$g_{GPL}^* = 0.8\%$	$g_{GPL}^* = 1\%$	$g_{GPL}^* = 1.2\%$
Uniaxial compression ($\times 10^4$)	Present	35.1	58.4	81.8	105.1	128.4	151.7	175
			166.3%	233%	299.4%	365.8%	432.1%	498.5%
	Song et al.[26]	35	58	82	105	128	152	175
			165.7%	234.3%	300%	365.7%	434.3%	500%
Biaxial compression ($\times 10^4$)	Present	17.5	29.2	40.9	52.5	64.2	75.8	87.5
			166.8%	233.7%	300%	366.8	433.1	500%
	Song et al.[26]	18	29	41	53	64	76	88
			161.1%	227.8%	294.4%	355.6%	422.2%	488.9%

5. Conclusions

In this paper, the Buckling behavior of three interior marine sandwich wall structure Types with rectangular, honeycomb, and re-entrant metamaterial cores was investigated based on a new fifth-order shear deformation theory. The effect of all three core shapes is established critical buckling loads as covered with multilayer graphene nanoplatelet (GPL)/polymer composite facesheets. The Halpin-Tsai model and the rule of the mixture were employed to achieve the effective material properties of facesheets. The Galerkin method was implemented to solve the governing equations of the sandwich walls that were derived using Hamilton's principle. The accurate results show that the presented fifth-order shear deformation theory is efficient in predicting the Buckling of sandwich wall structures. Numerical results have shown a significant increase in the critical buckling load with an increase in the mass fraction of GNPs. With constant l_{GPL} , decreasing the h_{GPL} will increase the dimensionless critical buckling load, while increasing the w_{GPL} will decrease it. Generally, the value of the dimensionless critical buckling load of sandwich wall Type B is higher than that of the other Types with different core shapes. It is possible to increase the dimensionless critical buckling load of plate Type C by increasing the length of the vertical to inclined cell rib ratio (γ_1) in the core layer, while it is the opposite in the other two types. When a very small amount of GPLs is added to the polymer matrix, the critical buckling load can be increased significantly. The critical buckling load in all types is increased when the length-to-thickness ratio (a/H) is increased and it is increased at low values of the aspect ratio (a/b).

Nomenclature

- a Length of plate
- b Width of plate

- H Total thickness
- h_c Thickness of the core layer
- V_{GPL} GPL volume fraction
- ζ_T size parameter of GPL nanofillers
- ζ_L geometry parameter of GPL nanofillers
- E_{GPL} Young's modulus of the GPLs
- E_m Young's modulus of the polymer matrix
- w_{GPL} average width of the GPLs
- h_{GPL} average Thickness of the GPLs
- l_{GPL} average length of the GPLs
- ν_c effective Poisson's ratio of facesheets
- ρ_c Mass density
- γ_1 Length ratio of cell ribs
- γ_2 Thickness ratio of cell ribs
- γ_3 Length to Thickness of cell ribs
- I_j Plate inertias
- ϵ_{ij} Normal strains
- σ_{ij} Normal stresses
- U,V,W Displacement components
- t1, t2 Thickness of ribs of auxetic's cell
- L1, L2 Length of ribs of auxetic's cell
- \bar{N}_{cr} Dimensionless critical buckling load

Reference

[1] Boh, J.W., Louca, L.A., Choo, Y.S. & Mouring, S.E., 2005. Damage modelling of scrimp woven roving laminated beams subjected to transverse shear. *Composites Part B: Engineering*, 36 (5), pp.427-438.

[2] Di Bella, G., Calabrese, L. & Borsellino, C., 2012. Mechanical characterisation of a glass/polyester sandwich structure for

- marine applications. *Materials & Design*, 42, pp.486-494.
- [3] Palomba, G., Epasto, G. & Crupi, V., 2021. Lightweight sandwich structures for marine applications: A review. *Mechanics of Advanced Materials and Structures*, pp.1-26.
- [4] Birman, V. & Kardomateas, G.A., 2018. Review of current trends in research and applications of sandwich structures. *Composites Part B: Engineering*, 142, pp.221-240.
- [5] Tarlochan, F., Ramesh, S. & Harpreet, S., 2012. Advanced composite sandwich structure design for energy absorption applications: Blast protection and crashworthiness. *Composites Part B: Engineering*, 43 (5), pp.2198-2208.
- [6] Belingardi, G., Cavatorta, M.P. & Duella, R., 2003. Material characterization of a composite-foam sandwich for the front structure of a high speed train. *Composite Structures*, 61 (1), pp.13-25.
- [7] Crupi, V., Epasto, G. & Guglielmino, E., 2013. Comparison of aluminium sandwiches for lightweight ship structures: Honeycomb vs. Foam. *Marine Structures*, 30, pp.74-96.
- [8] Kortenoeven, J., Boon, B. & De Bruijn, A., 2008. Application of sandwich panels in design and building of dredging ships. *Journal of Ship Production*, 24 (03), pp.125-134.
- [9] Montazeri, A. & Rafii-Tabar, H., 2011. Multiscale modeling of graphene- and nanotube-based reinforced polymer nanocomposites. *Physics Letters A - PHYS LETT A*, 375, pp.4034-4040.
- [10] Potts, J.R., Dreyer, D.R., Bielawski, C.W. & Ruoff, R.S., 2011. Graphene-based polymer nanocomposites. *Polymer*, 52 (1), pp.5-25.
- [11] Rafiee, M.A., Rafiee, J., Srivastava, I., Wang, Z., Song, H., Yu, Z.Z. & Koratkar, N., 2010. Fracture and fatigue in graphene nanocomposites. *Small*, 6 (2), pp.179-83.
- [12] Rafiee, M.A., Rafiee, J., Wang, Z., Song, H., Yu, Z.-Z. & Koratkar, N., 2009. Enhanced mechanical properties of nanocomposites at low graphene content. *ACS Nano*, 3 (12), pp.3884-3890.
- [13] Rafiee, M.A., Rafiee, J., Yu, Z.-Z. & Koratkar, N., 2009. Buckling resistant graphene nanocomposites. *Applied Physics Letters*, 95 (22), pp.223103.
- [14] Imani Yengejeh, S., Kazemi, S.A. & Öchsner, A., 2017. Carbon nanotubes as reinforcement in composites: A review of the analytical, numerical and experimental approaches. *Computational Materials Science*, 136, pp.85-101.
- [15] Kolahchi, R. & Moniri Bidgoli, A.M., 2016. Size-dependent sinusoidal beam model for dynamic instability of single-walled carbon nanotubes. *Applied Mathematics and Mechanics*, 37 (2), pp.265-274.
- [16] Mehar, K., Panda, S.K. & Mahapatra, T.R., 2017. Theoretical and experimental investigation of vibration characteristic of carbon nanotube reinforced polymer composite structure. *International Journal of Mechanical Sciences*, 133, pp.319-329.
- [17] Mittal, G., Dhand, V., Rhee, K.Y., Park, S.-J. & Lee, W.R., 2015. A review on carbon nanotubes and graphene as fillers in reinforced polymer nanocomposites. *Journal of Industrial and Engineering Chemistry*, 21, pp.11-25.
- [18] Palomba, G., Epasto, G., Sutherland, L. & Crupi, V., 2021. Aluminium honeycomb sandwich as a design alternative for lightweight marine structures. *Ships and Offshore Structures*, pp.1-12.
- [19] Bitzer, T., 1994. Honeycomb marine applications. *Journal of Reinforced Plastics and Composites*, 13 (4), pp.355-360.
- [20] Burton, W.S. & Noor, A.K., 1997. Assessment of continuum models for sandwich panel honeycomb cores. *Computer Methods in Applied Mechanics and Engineering*, 145 (3), pp.341-360.
- [21] Yang, J., Chen, D. & Kitipornchai, S., 2018. Buckling and free vibration analyses of functionally graded graphene reinforced porous nanocomposite plates based on chebyshev-ritz method. *Composite Structures*, 193, pp.281-294.
- [22] Kiani, Y., 2018. Nurbs-based isogeometric thermal postbuckling analysis of temperature dependent graphene reinforced composite laminated plates. *Thin-Walled Structures*, 125, pp.211-219.
- [23] Li, K., Wu, D., Chen, X., Cheng, J., Liu, Z., Gao, W. & Liu, M., 2018. Isogeometric analysis of functionally graded porous plates reinforced by graphene platelets. *Composite Structures*, 204, pp.114-130.
- [24] Ji, W. & Waas, A.M., 2010. 2d elastic analysis of the sandwich panel buckling problem: Benchmark solutions and accurate finite element formulations. *Zeitschrift für angewandte Mathematik und Physik*, 61 (5), pp.897-917.
- [25] Song, M., Yang, J., Kitipornchai, S. & Zhu, W., 2017. Buckling and postbuckling of biaxially compressed functionally graded multilayer graphene nanoplatelet-reinforced polymer composite plates. *International Journal of Mechanical Sciences*, 131-132, pp.345-355.
- [26] Song, M., Yang, J. & Kitipornchai, S., 2018. Bending and buckling analyses of functionally graded polymer composite plates reinforced with graphene

- nanoplatelets. *Composites Part B: Engineering*, 134, pp.106-113.
- [27] Shen, H.-S., Xiang, Y., Lin, F. & Hui, D., 2017. Buckling and postbuckling of functionally graded graphene-reinforced composite laminated plates in thermal environments. *Composites Part B: Engineering*, 119, pp.67-78.
- [28] Shahverdi, H., Barati, M.R. & Hakimelahi, B., 2019. Post-buckling analysis of honeycomb core sandwich panels with geometrical imperfection and graphene reinforced nanocomposite face sheets. *Materials Research Express*, 6 (9), pp.095017.
- [29] Arshid, E., Amir, S. & Loghman, A., 2021. Thermal buckling analysis of fg graphene nanoplatelets reinforced porous nanocomposite mcst-based annular/circular microplates. *Aerospace Science and Technology*, 111, pp.106561.
- [30] Song, M., Kitipornchai, S. & Yang, J., 2017. Free and forced vibrations of functionally graded polymer composite plates reinforced with graphene nanoplatelets. *Composite Structures*, 159, pp.579-588.
- [31] Shabani, Y. & Khorshidi, K., 2022. Free vibration analysis of rectangular doubly curved auxetic-core sandwich panels integrated with cnt-reinforced composite layers using galerkin method. *Journal of Science and Technology of Composites*, pp.-.
- [32] Fallah, A. & Khorshidi, K., 2019. The effect of nonlinear temperature distribution on the vibrational behavior of a size-dependent fg laminated rectangular plates undergoing prescribed overall motion. *Polymer Composites*, 40 (2), pp.766-778.
- [33] Khorshidi, K. & Shabani, Y., 2022. Free vibration analysis of sandwich plates with magnetorheological smart fluid core by using modified shear deformation theory. *Journal of Science and Technology of Composites*, pp.-.
- [34] Touratier, M., 1991. An efficient standard plate theory. *International Journal of Engineering Science*, 29 (8), pp.901-916.
- [35] Mantari, J.L., Oktem, A.S. & Guedes Soares, C., 2012. A new trigonometric shear deformation theory for isotropic, laminated composite and sandwich plates. *International Journal of Solids and Structures*, 49 (1), pp.43-53.
- [36] Soldatos, K.P., 1992. A transverse shear deformation theory for homogeneous monoclinic plates. *Acta Mechanica*, 94 (3), pp.195-220.
- [37] Reissner, E., 1975. On transverse bending of plates, including the effect of transverse shear deformation. *International Journal of Solids and Structures*, 11 (5), pp.569-573.
- [38] Ghasemi, A.R. & Mohandes, M., 2020. Free vibration analysis of micro and nano fiber-metal laminates circular cylindrical shells based on modified couple stress theory. *Mechanics of Advanced Materials and Structures*, 27 (1), pp.43-54.
- [39] Nejati, M., Ghasemi-Ghalebahman, A., Soltanimaleki, A., Dimitri, R. & Tornabene, F., 2019. Thermal vibration analysis of sma hybrid composite double curved sandwich panels. *Composite Structures*, 224, pp.111035.
- [40] Khorshidi, K. & Fallah, A., 2017. Free vibration analysis of size-dependent, functionally graded, rectangular nano/micro-plates based on modified nonlinear couple stress shear deformation plate theories. *Mechanics of Advanced Composite Structures*, 4 (2), pp.127-137.
- [41] Khorshidi, K., Taheri, M. & Ghasemi, M., 2020. Sensitivity analysis of vibrating laminated composite rec-tangular plates in interaction with inviscid fluid using efast method. *Mechanics of Advanced Composite Structures*, 7 (2), pp.219-231.
- [42] Khorshidi, K. & Farhadi, S., 2013. Free vibration analysis of a laminated composite rectangular plate in contact with a bounded fluid. *Composite Structures*, 104, pp.176-186.
- [43] Khorshidi, K., Bahrami, M., Eshaghi, M. & Ghasemi, M., 2021. A comprehensive nonlocal surface-piezoelectricity model for thermal and vibration analyses of piezoelectric nanoplates. *Composite Structures*, 263, pp.113654.